International Journal of Heat and Mass Transfer 52 (2009) 3850–3856

Contents lists available at ScienceDirect

International Journal of Heat and Mass Transfer

journal homepage: www.elsevier.com/locate/ijhmt

Buoyancy-induced flow in an open-ended cavity: Assessment of a similarity solution and of numerical simulation models

S.K.S. Boetcher [a], E.M. Sparrow [b,*]

[a] Department of Mechanical and Energy Engineering, Center for Advanced Scientific Computing and Modeling (CASCaM), University of North Texas, Denton, TX 76207-7102, USA
[b] Laboratory for Heat Transfer Practice, Department of Mechanical Engineering, University of Minnesota, Minneapolis, MN 55455-0111, USA

ARTICLE INFO

Article history:
Received 10 October 2008
Received in revised form 12 October 2008
Accepted 12 October 2008
Available online 7 April 2009

Keywords:
Buoyant flow
Open-ended cavity
Similarity solution
Numerical simulation
Nusselt numbers

ABSTRACT

The buoyancy-induced flow in a horizontal open-ended cavity has been investigated from three perspectives: (a) assessment of the validity of an existent similarity solution, (b) computational issues relevant to numerical simulation, and (c) obtainment and presentation of results of practical utility. Parameter ranges were sought within which the similarity solution might be valid, but no such ranges could be identified. The inapplicability of the similarity model may be attributed to the neglect of the streamwise second derivatives in the governing conservation equations and to the model's inability to accommodate boundary conditions at the opening of the channel. The numerical issues that were dealt with included the proper extension of the solution domain into the far field external to the channel, the appropriate boundary conditions on the surfaces of the extended domain, and meshing to achieve high accuracy. Local Nusselt numbers and their variation along the walls of the channel are presented.

1. Introduction

The past quarter century has seen an evolving literature dealing with a pair of closely related natural convection problems involving the buoyancy-driven interaction of fluid in a semi-confined space with fluid in an extensive external space. One of these problems, often termed the open-ended cavity, is a horizontal parallel-walled channel that is open at both ends and which interacts with an extensive space adjacent to the respective ends. The second problem is either called the partially open cavity or the open cavity. It consists of a horizontal channel closed at one end and open to an extensive space at its other end. The applications of these fundamental problems include electronic equipment cooling, fire incidents in internal spaces, chemical vapor deposition systems, solar collectors, and nuclear reactor incidents.

An early and truly seminal contribution to this problem area is that of Bejan [1]. Following a model for buoyant flow in a vertical, open thermosyphon due to Lighthill [2], Bejan developed a solution for the fluid flow and heat transfer within an open cavity without having to take account of the fluid in the space external to the cavity. The solution was actually a similarity solution, generically related to the celebrated Blasius solution for forced convection flow over a flat plate. In both these cases, the basic two-dimensional partial differential equations which govern the respective problems are reduced to ordinary differential equations by a similarity transformation.

Notwithstanding the elegance of similarity solutions, it is widely understood that they have numerous practical limitations which restrict their applicability. For instance, for the venerable Blasius flat-plate problem, there are both Reynolds and Prandtl number (for heat transfer) limitations in addition to the plate thinness requirement.

One of the goals of the present investigation is to define the parametric ranges of applicability of the Bejan similarity solution for the open cavity. The dimensionless parameters that characterize the problem are the Rayleigh number, Prandtl number, and the cavity aspect ratio. This goal will be achieved by a benchmark-quality numerical simulation of the problem.

Another goal of this work is to deal definitively with three issues which have impacted prior numerical simulations of the problem. They are: (a) the extension of the solution domain into the external space adjacent to the cavity opening(s), (b) the boundary conditions applied to the surfaces of the extended domain, and (c) the mesh density used in the numerical solutions.

The extended solution domains used by Penot [3] and by Chan and Tien [4] were inappropriately small. In addition, the grid density (800 and 2000 elements, respectively) is insufficient when judged by current standards. In addition, the boundary conditions applied to the surfaces of the extended domain do not express reality. Vafai and Ettefagh [5] demonstrated the importance of a large extended solution domain. The boundary conditions applied to the surfaces of the extended domain are those presently regarded as

* Corresponding author. Tel.: +1 612 625 5502.
E-mail address: esparrow@umn.edu (E.M. Sparrow).

0017-9310/$ - see front matter © 2009 Elsevier Ltd. All rights reserved.
doi:10.1016/j.ijheatmasstransfer.2008.10.035

Nomenclature

c_p	specific heat
Gr	Grashof number, Eq. (2)
g	acceleration of gravity
H	height of cavity
h	heat transfer coefficient, Eq. (9)
k	thermal conductivity
L	length of channel
Nu	Nusselt number, Eq. (10)
n	surface normal
P	dimensionless pressure, Eq. (1)
p	pressure
Pr	Prandtl number, Eq. (2)
q	local heat flux
Ra	Rayleigh number, Eq. (2)
T	temperature
T_w	wall temperature
T_∞	far-field temperature
U, V	dimensionless velocities, Eq. (1)
u, v	velocity components
X, Y	dimensionless Cartesian coordinates, Eq. (1)
x, y	Cartesian coordinates
Greek	
β	coefficient of thermal expansion
θ	dimensionless temperature, Eq. (1)
μ	viscosity
ν	kinematic viscosity
ρ	density
ρ_∞	density in the far field
τ	temperature profile shape, Eq. (8)
ϕ'	velocity profile shape, Eq. (7)
Subscript	
pen	penetration depth

applicable to outflow boundaries, and the mesh density was not specified. Follow-on papers by Khanafer and Vafai [6,7] also imposed outflow conditions on the boundaries of the extended solution domain. These authors also attempted to find a set of fictive boundary conditions to be applied at the open end of the cavity whose use would obviate the need for an extended solution domain. However, according to Icoz and Jaluria [8], these fictive boundary conditions are applicable only to specific geometries and limited flow conditions.

The focus of the aforementioned Icoz–Jaluria paper was an open-ended channel with heat sources protruding into the channel. The solution domain was not extended into the space external to the channel. Very recently, Andreozzi et al. [9] numerically investigated an open-ended cavity having thermal boundary conditions different from those of preceding studies. An extended solution domain of unspecified size was used, but the schematic diagram of the problem, if to scale, suggests possible sizewise insufficiency. The boundary conditions applied at the surfaces of the extended domain totally precluded vertical flow there.

The simulation model used here eliminates all of the issues of uncertainty that were identified in the preceding paragraphs and, thereby, provides results of impeccable accuracy.

2. The solution domain and boundary conditions

A schematic diagram of the open cavity and of the adjacent fluid environment is exhibited in Fig. 1. The diagram also shows, as a dashed-line closed contour, the solution domain within which the numerical simulations are to be performed. Consistent with the two-dimensional model displayed in the figure, the coordinates are x and y, and the length and height dimensions of the cavity are L and H, respectively. The cavity aspect ratio AR is equal to L/H. The extended solution domain, the rectangle $ABCDA$, is much larger in size than the cavity proper in accordance with the concerns discussed earlier. In particular, the width and total height of the extended domain are $10H$ and $18H$, respectively.

The boundary conditions at the walls of the cavity proper were selected to facilitate the assessment of the validity of the similarity solution of [1]. The no-slip and impermeability conditions require that the velocity components u and v are zero on all the cavity walls. In addition, all of the walls of the cavity are isothermal at a common temperature T_w.

The vertical walls that flank the cavity opening from above and below are adiabatic and are also surfaces of zero velocity. In the external environment at locations sufficiently far from the cavity opening, the temperature is T_∞, and the velocities are vanishingly small. The application of these far-field boundary conditions is not a straightforward matter and may have been mishandled in prior investigations.

In this regard, representative treatments of the far-field boundary conditions in the relevant published literature will be discussed. In one paper, the vertical velocity v was set equal to zero on all the bounding surfaces AB, BC, and CD of the extended solution domain (Fig. 1). This model totally blocked any fluid from entering the domain across CD and from leaving the domain across AB. At one of these boundaries, the temperature was assigned the value T_∞, while the other boundaries were specified as being adia-

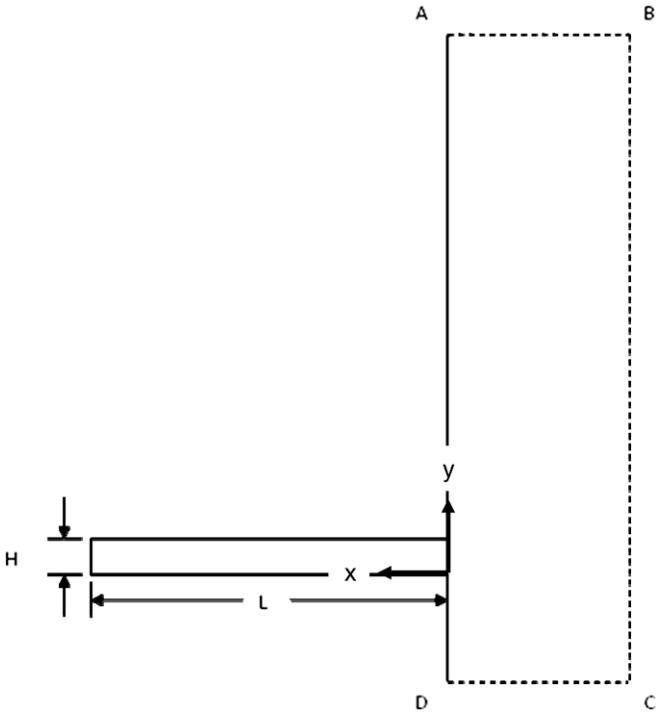

Fig. 1. Schematic diagram of the open cavity and the solution domain.

batic. These conditions are believed to be too inflexible to permit the natural fluid flow and thermal process to occur.

In other papers, adiabatic conditions were applied at all the boundaries *AB*, *BC*, and *CD*. These assignments preclude the specification of the environment temperature T_∞ at boundary locations at which there is fluid inflow. In still another paper, both velocity components were set equal to zero on *AB*, *BC*, and *CD*, and $T = T_\infty$ there. This is another case of conditions that were specified too strongly. In a unique treatment, boundary conditions were chosen primarily to provide more stable solutions and faster convergence.

The foregoing discussion casts a cloak of uncertainty on the preceding implementations of the far-field boundary conditions. The approach used here is tailored to enable natural fluid flow and thermal processes to occur in the far field. The implementation of this approach was accomplished by means of ANSYS CFX 11.0 software. In particular, the *opening* boundary condition permits the fluid to enter or leave across a boundary in accordance with the dynamics of the situation. If fluid passes into the solution domain across a boundary, the temperature is specified as T_∞ at the crossing point. At boundary locations where there is fluid outflow, the standard thermal outflow condition, zero second derivative of T with respect to the surface normal is imposed, where n is the surface normal. It is believed that the present far-field treatment closely models events in the far field.

To facilitate the numerical solution, the domain was meshed by means of ANSYS ICEM which is a meshing tool. This high-end mesher provides outstanding control of the discretization process. In particular, it was used to create a brick mesh, which is known to be the most accurate form of mesh. All told, the mesh consisted of 282,000 nodes and 140,000 elements.

The attainment of converged numerical solutions for buoyant flows is especially demanding when a significant portion of the solution domain is not bounded by walls, as is true in the present instance. The difficulty is aggravated at higher values of the Rayleigh number. The strategy used to cope with this situation was to initiate the solution task at the lowest Rayleigh number considered, namely, $Ra = 100$. For this Rayleigh number, and for a selected aspect ratio *AR*, a solution was obtained in which the normalized RMS values of the residuals attained values of at least 10^{-6} for all of the dependent variables. Then, for the same aspect ratio, attention was turned to $Ra = 1000$. The starting values for this case were taken from the converged solution for $Ra = 100$. The same approach was used to proceed to higher values of *Ra*.

The final set of solutions encompassed *Ra* values of 100, 1000, and 10,000 for each of four aspect ratios $AR = 2$, 5, 10, and 20.

3. The governing equations

The governing equations were cast in dimensionless form for computational convenience, and the dimensionless variables and parameters are defined in Eqs. (1) and (2). The buoyancy term that appears in the *Y*-momentum equation is based on the Boussinesq equation of state. Aside from the density variation that underlies the buoyancy term, all the thermophysical properties are constant.

$$(U,V)=\frac{(u,v)}{\nu/H},\quad (X,Y)=\frac{(x,y)}{H},\quad P=\frac{p+\rho_\infty gy}{\rho(\nu/H)^2},\quad \theta=\frac{T-T_\infty}{T_w-T_\infty} \tag{1}$$

$$Gr=\frac{g\beta(T_w-T_\infty)H^3}{\nu^2},\quad Pr=\frac{c_p\mu}{k},\quad Ra=GrPr \tag{2}$$

Conservation of mass

$$\frac{\partial U}{\partial X}+\frac{\partial V}{\partial Y}=0 \tag{3}$$

Conservation of *X*-momentum

$$\frac{\partial U^2}{\partial X}+\frac{\partial (UV)}{\partial Y}=-\frac{\partial P}{\partial X}+\frac{\partial^2 U}{\partial X^2}+\frac{\partial^2 U}{\partial Y^2} \tag{4}$$

Conservation of *Y*-momentum

$$\frac{\partial (UV)}{\partial X}+\frac{\partial V^2}{\partial Y}=-\frac{\partial P}{\partial Y}+\frac{\partial^2 V}{\partial X^2}\frac{\partial^2 V}{\partial Y^2}+Gr\theta \tag{5}$$

Conservation of energy

$$\frac{\partial (U\theta)}{\partial X}+\frac{\partial (V\theta)}{\partial Y}=\frac{1}{Pr}\left[\frac{\partial^2\theta}{\partial X^2}+\frac{\partial^2\theta}{\partial Y^2}\right] \tag{6}$$

4. Results and discussion

Three categories of results will be presented and discussed. The focus of the first category is to assess the validity of the similarity solution of [1]. In the second category of results, representative patterns of fluid flow will be exhibited. Also presented in this category is the penetration distance of the external air into the cavity. The third category conveys heat transfer results at the bounding walls of the cavity.

4.1. Similarity issues

The key assumptions that underlie the similarity model of [1] are that the respective shapes of the velocity and temperature profiles are independent of the longitudinal position in the cavity. In [1], the shape of the profile of the streamwise velocity u (or U) is expressed by the function $\phi'(Y)$. From the numerical solutions obtained here, $\phi'(Y)$ may be evaluated from

$$\phi'=\left[\frac{U}{X_{pen}-X}\right]Pr \tag{7}$$

In this equation, U is the dimensionless streamwise velocity which is a function of X and Y. The quantity X_{pen} is the dimensionless distance from the cavity opening to which the buoyancy-driven flow penetrates into the cavity, and X is the dimensionless streamwise coordinate measured from the cavity opening (Fig. 1). The Prandtl number Pr was taken to be 0.7 which corresponds to air and other gases.

The quantity ϕ' was evaluated from Eq. (7) as a function of X and Y for all 12 of the cases dealt with here. However, in view of space limitations, only representative results will be presented. To this end, Figs. 2–5 have been prepared. These figures are for $Ra = 1000$ (the intermediate *Ra* value considered here) and for

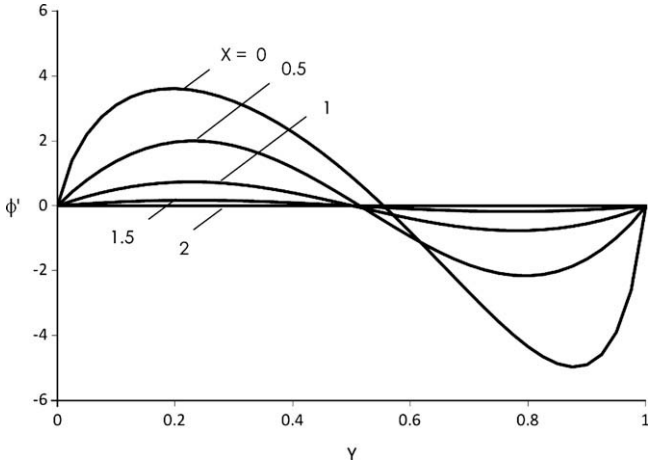

Fig. 2. Profiles of ϕ' at various streamwise locations for $AR = 2$ and $Ra = 1000$.

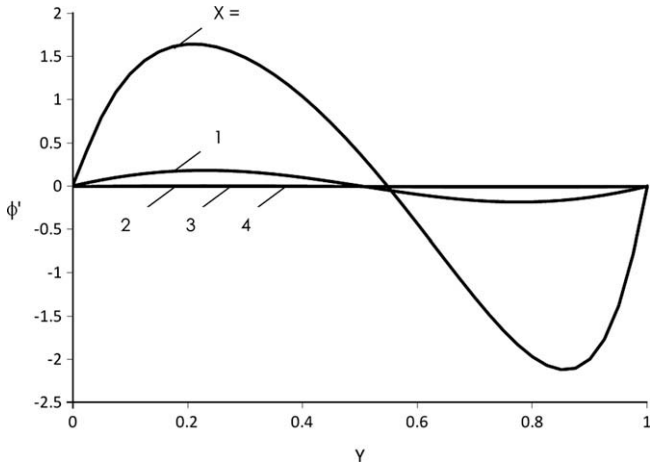

Fig. 3. Profiles of ϕ' at various streamwise locations for $AR = 5$ and $Ra = 1000$.

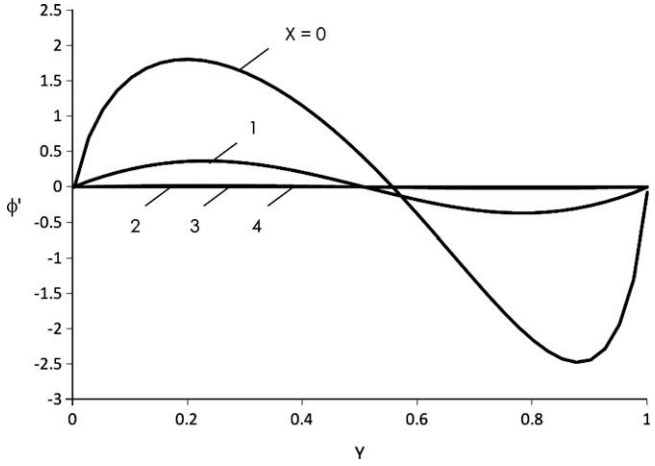

Fig. 4. Profiles of ϕ' at various streamwise locations for $AR = 10$ and $Ra = 1000$.

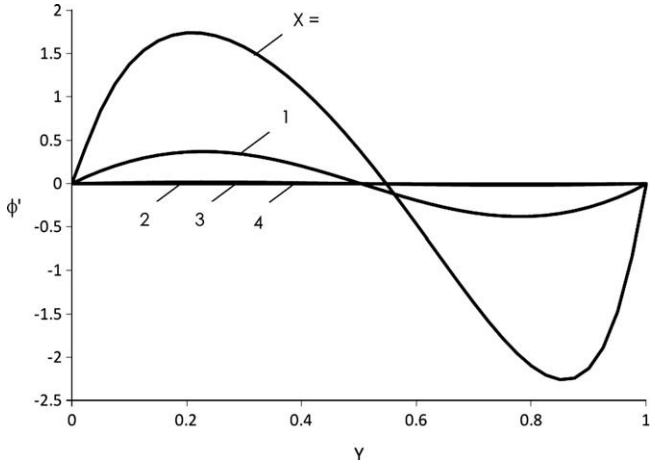

Fig. 5. Profiles of ϕ' at various streamwise locations for $AR = 20$ and $Ra = 1000$.

aspect ratios $AR = 2$, 5, 10, and 20. In each figure, profiles of ϕ' versus Y are plotted for parametric values of X between 0 and X_{pen}.

For the assessment of these figures, it is relevant to recall that the basis of the similarity model of [1] is that ϕ' depends only on Y and is independent of X. The results set forth in the figures do not support this model. Clearly, ϕ' is a strong function of X, with the largest ϕ' values occurring at $X = 0$ and the smallest at $X = X_{pen}$.

Other figures, respectively, for $Ra = 100$ and 10,000 and for $AR = 2$, 5, 10, and 20, display behaviors identical to those in evidence in Figs. 2–5. On this basis, it may be concluded that the similarity model is not valid for $100 < Ra < 10{,}000$ and $2 < AR < 20$.

The other tenet which underlies the similarity model of [1] is that the shape of the temperature profiles is a unique function of the cross-sectional coordinate Y and is independent of the longitudinal coordinate X. In the notation of [1], the temperature shape function is denoted by $\tau(Y)$. In terms of the variables of the present analysis,

$$\tau = \frac{(\theta - 1)Ra}{(X_{pen} - X)^2} \tag{8}$$

Eq. (8) was used in conjunction with the present numerical solutions to evaluate τ as a function of X and Y for all 12 of the investigated cases. Once again, it is sufficient to display representative results as conveyed in Figs. 6–9. These figures correspond to $Ra = 1000$ and to $AR = 2$, 5, 10, and 20, the same cases as parameterized Figs. 2–5. In each figure, τ is plotted as a function of Y for parametric values of X.

The critical issue to be considered in the appraisal of Figs. 6–9 is the marked dependence of τ on X. This X-dependence contradicts the $\tau = \tau(Y)$ assumption that underlies the similarity model of [1]. Figures that correspond to the other eight cases considered here show X-dependences that are similar to those seen in Figs. 6–9. These findings reinforce the aforementioned conclusion about the inappropriateness of the similarity model for the ranges of Ra and AR investigated here.

4.2. Patterns of fluid flow

A display of representative fluid-flow patterns is presented in Figs. 10–13 in the form of streamlines. The successive figures correspond to $Ra = 1000$ and to $AR = 2$, 5, 10, and 20. Each figure exhibits a to-scale depiction of the solution domain which includes the heated channel and the space external to the channel opening. Note that the encompassed external space is the same for all of the figures but that the channel becomes elongated with increasing values of the aspect ratio AR.

Attention will first be turned to the streamlines that depict the pattern of fluid flow within the channel proper and in the external

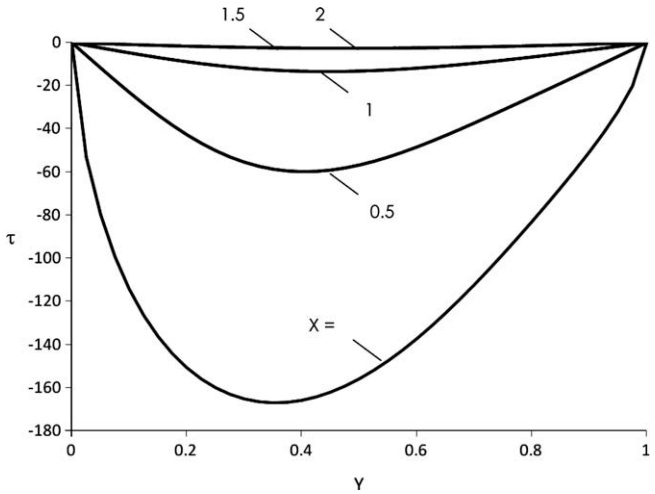

Fig. 6. Profiles of τ at various streamwise locations for $AR = 2$ and $Ra = 1000$.

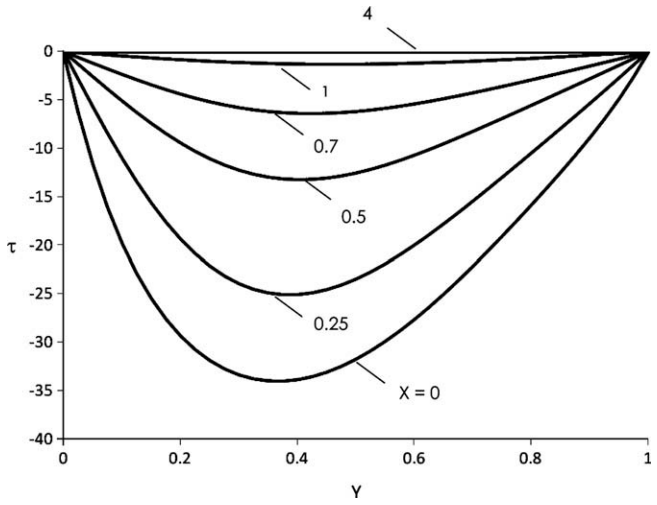

Fig. 7. Profiles of τ at various streamwise locations for $AR = 5$ and $Ra = 1000$.

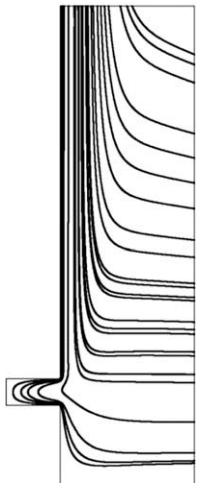

Fig. 10. Streamline patterns for $AR = 2$ and $Ra = 1000$.

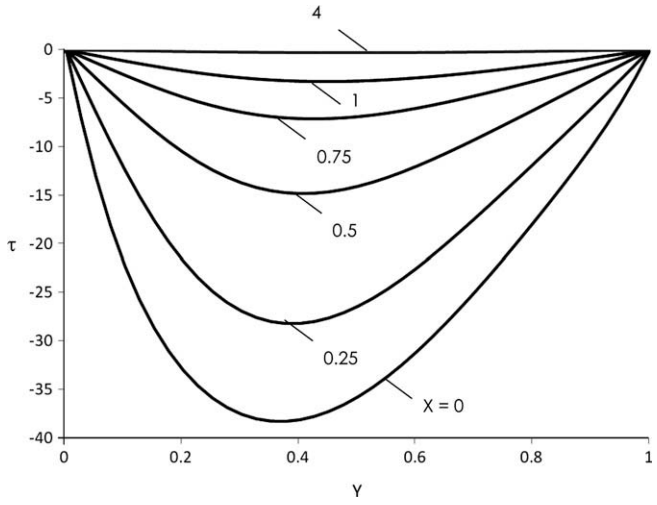

Fig. 8. Profiles of τ at various streamwise locations for $AR = 10$ and $Ra = 1000$.

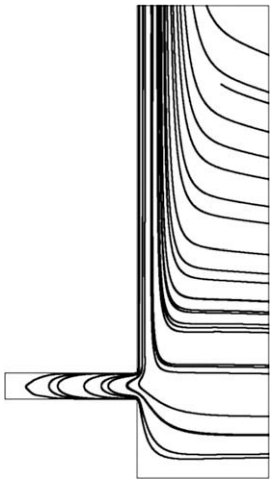

Fig. 11. Streamline patterns for $AR = 5$ and $Ra = 1000$.

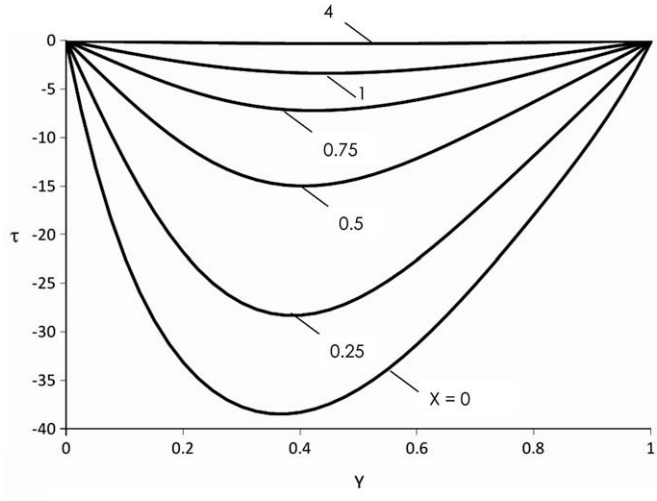

Fig. 9. Profiles of τ at various streamwise locations for $AR = 20$ and $Ra = 1000$.

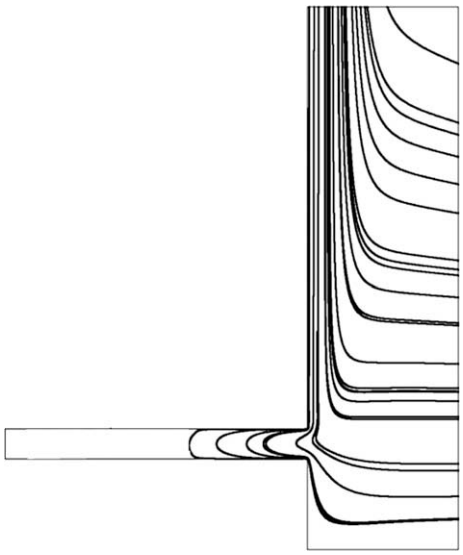

Fig. 12. Streamline patterns for $AR = 10$ and $Ra = 1000$.

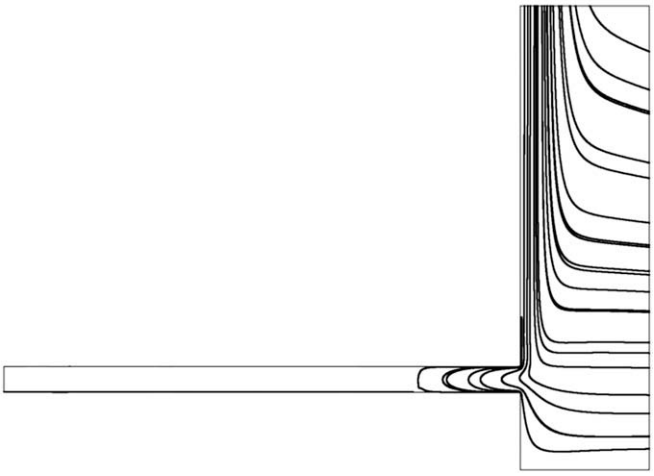

Fig. 13. Streamline patterns for $AR = 20$ and $Ra = 1000$.

space immediately adjacent to the channel opening. Of particular note is the depth to which the flow penetrates into the channel. For $AR = 2$, the penetration is complete in that the moving fluid washes over the wall which bounds the closed end of the channel. However, for all the other aspect ratios (5, 10, and 20), total penetration is no longer achieved. In fact, for these cases, the penetration depth is virtually independent of the aspect ratio.

The latter observation is reinforced by the information that is conveyed in Table 1, where dimensionless penetration depths X_{pen} are listed as functions of Ra and AR. Not unexpectedly, there is a tendency of the penetration depth to increase with increasing Rayleigh number.

Focus may now be returned to Figs. 10–13 and to the flow patterns in the neighborhood of the channel inlet. From the streamline shapes, it can be inferred that the flow which enters the channel from below possesses both axial and cross-stream (i.e., vertical) velocity components.

A similar inference follows from inspection of the streamlines of the fluid leaving the channel. These observations can be contrasted with the streamline pattern based on the similarity model of [1]. Inspection of the streamlines displayed in Fig. 5 of [1] reveals a strictly axial inflow and outflow at the channel inlet. This departure from reality is due to the total neglect of the space external to the channel in the similarity model.

Figs. 10–13 show that the flow entering the channel comes from the portion of the external space that is situated at elevations lower than that of the channel opening. The buoyant fluid leaving the channel initiates a boundary flow along the vertical wall which extends upward from the channel opening. The boundary layer is thickened by means of entrainment of fluid from the farther reaches of the external space.

4.3. Nusselt numbers

The quantity of most direct practical utility is the heat transfer coefficient and its variation along the walls of the channel. The local heat transfer coefficient is defined as

Table 1
Penetration depths X_{pen}.

	Aspect ratio			
Ra	2	5	10	20
10^2	2.00	3.50	3.50	3.50
10^3	2.00	4.00	4.00	4.00
10^4	2.00	4.25	4.25	4.25

$$h = \frac{q}{T_w - T_\infty} \tag{9}$$

where q is the local heat flux. A dimensionless presentation of h is made by means of the local Nusselt number Nu, where

$$Nu = \frac{hH}{k} \tag{10}$$

The Nusselt number results are presented in Figs. 14–17, which respectively correspond to aspect ratios $AR = 2$, 5, 10, and 20. Each figure contains six curves. The three dashed curves represent the Nusselt number values at the lower wall of the channel, while the continuous curves are for the upper-wall Nusselt numbers. That the lower-wall Nusselt numbers exceed those of the upper wall is consistent with the streamline patterns of Figs. 10–13. Those figures show that the fluid washing over the lower wall comes from the external environment whose temperature, T_∞, is the lowest temperature of the system. On the other hand, the fluid that washes over the upper wall has been preheated from its contact with the lower wall.

The variation of the Nusselt number along the length of the channel walls reflects the impacts of two processes. First, due to the heat absorbed by the fluid as it penetrates the channel, the local wall-to-fluid temperature difference decreases with increasing distance from the channel opening. This process gives rise to the decreasing values of the Nusselt number with x. The second process relates to the local maximum in each one of the Nusselt number distributions. These maxima occur very near the channel inlet (i.e., at small x). The shape of the Nusselt number curves in this region is a clear indicator of the presence of a recirculation zone. It is well established that the local maximum is related to the reattachment of the separated flow to the wall. As expected, the higher the Rayleigh number, the higher is the Nusselt number. However, the role of the aspect ratio merits some discussion. In this regard, note that for $AR = 2$, Fig. 14, the abscissa variable is x/L, whereas for the other aspect ratios, Figs. 15–17, the abscissa is x/x_{pen}. This distinction reflects the fact that the fluid fully penetrates the $AR = 2$ channel whereas only partial penetration occurs for the other aspect ratios. Thus, there is active heat transfer over all along the channel walls for $AR = 2$, but not for the other cases. It is interesting to note that since the Nusselt number maxima occurs near the channel opening, the magnitudes of the maxima are insensitive to the aspect ratio.

5. Concluding remarks

The goals of this research are to (a) assess the validity of a similarity-solution model of the problem, (b) deal definitively with

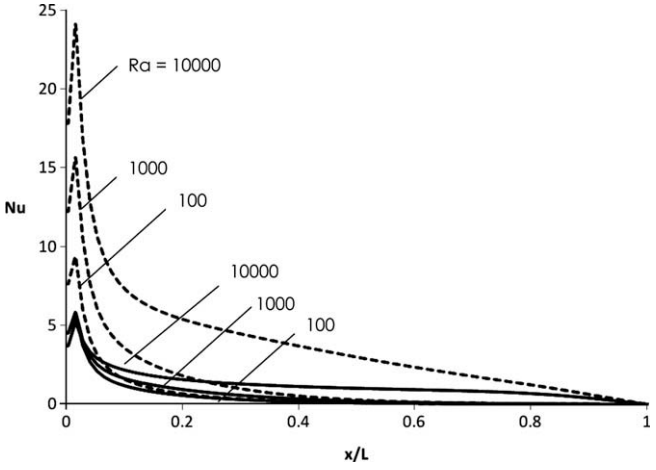

Fig. 14. *Nu* numbers for various *Ra* numbers for $AR = 2$.

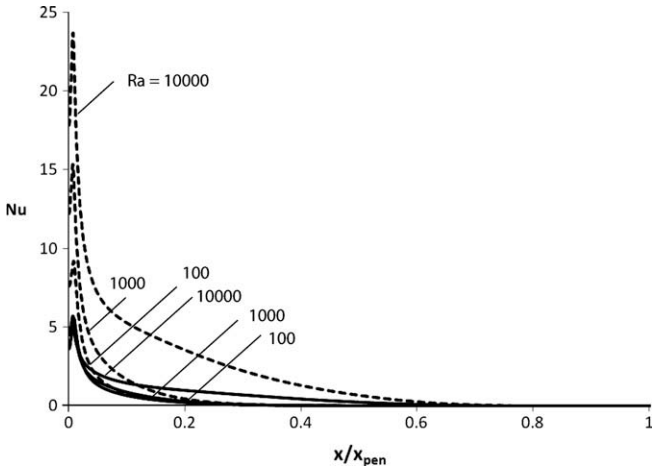

Fig. 15. *Nu* numbers for various *Ra* numbers for *AR* = 5.

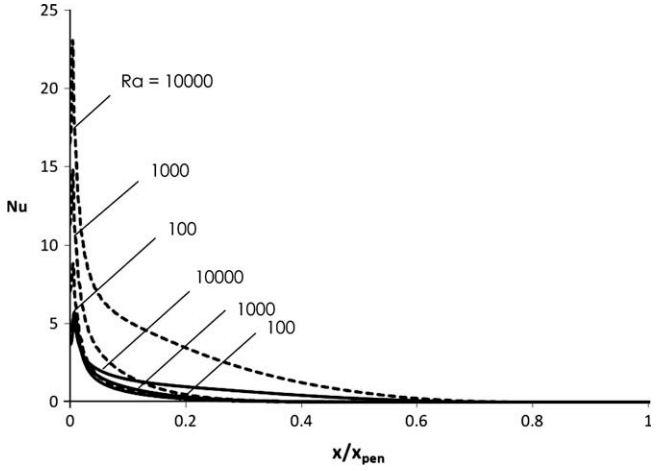

Fig. 16. *Nu* numbers for various *Ra* numbers for *AR* = 10.

critical issues related to the numerical simulation of the problem, and (c) provide results of practical utility.

The similarity-solution model is, in effect, a boundary-layer model. As is usual in such models, the streamwise second derivatives are omitted. Of perhaps greater significance is that the boundary conditions at the channel opening have to be left unspecified in the similarity model. As a consequence, the flow within the channel is totally uninformed about any happenings which might occur in the space external to the channel.

When this work was undertaken, the initial intent was to determine the ranges of the relevant parameters for which the similarity solutions would be valid. However, as demonstrated in Figs. 2–9, it was not possible, within the ranges examined here, to find any

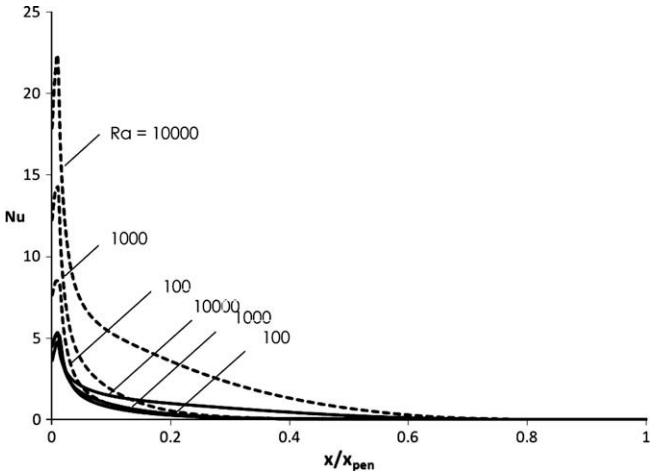

Fig. 17. *Nu* numbers for various *Ra* numbers for *AR* = 20.

conditions for which the similarity model is valid. In particular, according to the similarity model, the function ϕ' should be independent of the horizontal coordinate *x*, which clearly is not supported by the results of Figs. 2–9.

The simulation issues of interest are the size of the external solution domain, the use of appropriate boundary conditions on the surfaces of the external solution domain, and the mesh density. All of these issues have been rectified in the present simulation.

Numerical results are presented for the local Nusselt number and its variation along the walls of the channel. In general, the highest Nusselt number values occur near the channel opening. The shape of the Nusselt number variation indicates a zone of flow separation near the opening of the channel.

References

[1] A. Bejan, S. Kimura, Penetration of free convection into a lateral cavity, J. Fluid Mech. 103 (1981) 465–478.
[2] M.J. Lighthill, Theoretical considerations on free convection in tubes, Quart. J. Mech. Appl. Math. 6 (1953) 398–439.
[3] F. Penot, Numerical calculation of two-dimensional natural convection in isothermal open cavities, Numer. Heat Transfer 5 (1982) 421–437.
[4] Y.L. Chan, C.L. Tien, Numerical study of two-dimensional natural convection in square open cavities, Numer. Heat Transfer 8 (1985) 65–80.
[5] K. Vafai, J. Ettefagh, Thermal and fluid flow instabilities in buoyancy-driven flows in open-ended cavities, Int. J. Heat Mass Transfer 33 (1990) 2329–2344.
[6] K. Khanafer, K. Vafai, Buoyancy-driven flow and heat transfer in open-ended enclosures: elimination of the extended boundaries, Int. J. Heat Mass Transfer 43 (2000) 4087–4100.
[7] K. Khanafer, K. Vafai, Effective boundary conditions for buoyancy-driven flows and heat transfer in fully open-ended two-dimensional enclosures, Int. J. Heat Mass Transfer 45 (2003) 2527–2538.
[8] T. Icoz, Y. Jaluria, Numerical simulation of boundary conditions and the onset of instability in natural convection due to protruding thermal sources in an open rectangular channel, Numer. Heat Transfer A 48 (2005) 831–847.
[9] A. Andreozzi, Y. Jaluria, O. Manca, Numerical investigation of transient natural convection in a horizontal channel heated from the upper wall, Numer. Heat Transfer A 51 (2007) 815–842.